A LUNAR SPECTRAL FLUX DATABASE FOR QUANTITATIVE VIIRS DAY/NIGHT BAND ENVIRONMENTAL APPLICATIONS

Steven D. Miller[*]
Cooperative Institute for Research in the Atmosphere, Fort Collins, CO

Robert E. Turner
Scientific Applications International Corporation, Monterey, CA

1. INTRODUCTION

Visible-band (e.g., 0.4-0.7 μm) satellite radiometers are used almost exclusively for daytime observations, when a significant amount of sunlight reflection is available. Silicon photodetectors offer adequate sensitivity to a broad range of daytime visible light (e.g., 10^0 to 10^2 W/m^2-sr-μm). Examples of such sensors include the visible channels on the Advanced Very High Resolution Radiometer (AVHRR), the MODerate Resolution Imaging Spectroradiometer (MODIS), and the Geostationary Operational Environmental Satellite (GOES) imager.

Visible light is also prevalent during the nighttime hours, albeit at significantly lower levels or confined to relatively small. Nighttime lights typically require a very high degree of amplification to be detectable from the satellite platform. Examples of nighttime lights include both artificial (e.g., city lights, gas flares, fishing boat lights) and natural (moonlight, lightning, aurora, and bioluminescence) sources (e.g., Croft [1978]).

Of particular interest to nighttime environmental applications is the use of moonlight in the same way as the sun—enabling equivalent daytime applications which require measurements of visible reflectance. The requirement for doing so is an accurate specification of the downwelling top-of-atmosphere (TOA) lunar spectral irradiance (flux). Unlike the downwelling TOA solar flux, the lunar flux varies dramatically across the lunar cycle (new moon to full moon) and with sun/earth/moon (S/E/M) geometry.

This paper summarizes the development of a high resolution (1 nm) lunar spectral spectral flux model designed to enable quantitative applications from the calibrated Day/Night Band (DNB) to fly on board the National Polar-orbiting Operational Environmental Satellite System's (NPOESS) Visible/Infrared Imager/Radiometer Suite (VIIRS).

[*]*Corresponding author address:* Steven D. Miller, Cooperative Institute for Research in the Atmosphere (CIRA), Fort Collins, CO 80523; e-mail: miller@cira.navy.mil

2. THE VIIRS DAY/NIGHT BAND

The Defense Meteorological Satellite Program (DMSP) was the first to offer measurements of nighttime lights. A Department of Defense (DoD) program, the DMSP was designed in part to supply military analysts with a means to producing global cloud cover analyses during both day and night hours. One of its sensors, the Operational Linescan System (OLS) offers a two-band (0.6 μm visible and 11.0 μm thermal infrared window) imager useful for detection of low and high clouds. What makes the OLS unique is its extremely high sensitivity to low levels (e.g., down to 10^{-5} W/m^2-sr, band averaged radiance) of visible light, achieved via a high-gain amplifier (photomultiplier tube), enabling a wide assortment of low-light applications (e.g., Lee et al, 2006).

With its principle emphasis on contrast-based cloud detection, the OLS nighttime visible channel lacks attributes useful to quantitative applications. Its poor radiometric resolution (6-bit data; or 64 gray-shades) and unreported calibration (uses a dynamic, highly variable scene/swath/lunar-cycle dependant gain aimed at attaining maximum scene contrast; e.g., Elvidge,1999) relegate its practical usage to imagery. In addition, the OLS suffers from stray sunlight entering the telescope during certain parts of the season, causing diffuse light 'glare' effects which contaminate and render useless significant portions of the imagery swath.

The forthcoming NPOESS program (to launch in ~2014, with a preparatory project to launch in late 2009) will offer several new technologies—including an improved nighttime visible capability drawing heritage from the DMSP/OLS. The VIIRS sensor will provide 22 bands in the optical spectrum. Included in this suite is the DNB, which will capture a wider range of low-light signals at higher spatial and radiometric resolution than the OLS. The minimum radiance of the DNB (at highest stage gain and detector aggregation mode) is 10^{-5} W/m2-sr-um, similar to OLS. Where the DNB exceeds OLS performance is in both its spatial (0.74 km across entire swath) and radiometric (14-bit data) resolution. These

improvements will enable the first quantitative nighttime applications—a true paradigm shift in operational remote sensing capabilities.

3. KNOWLEDGE OF LIGHT 'INPUT'

A high fidelity measurement of reflected moonlight is of only limited use without some knowledge of how much light came into the system. We must first know the input light (i.e., down-welling flux) to compute scene reflectance which is then related to various physical properties of the reflecting environment. Without an accurate account for the lunar input, the DNB cannot realize its full potential as a nocturnal analog to the daytime visible channels.

For daytime visible-band sensors, the down-welling TOA solar spectral flux is well defined. In contrast, moonlight is a highly variable quantity. First, the moon is not a self-luminous object; it simply reflects sunlight impingent upon it. The illuminated portion of the moon (and its associated flux output) as viewed from the earth varies (waxes/wanes) across the lunar cycle. Second, the magnitude of TOA lunar flux at a given point in the lunar cycle varies from one cycle to the next (owing to the moon's own elliptical orbit) and across the seasons (elliptical moon/earth-system orbit around the sun). There are other factors (e.g., lunar libration) which complicate further the temporal irradiance output of the moon.

Lastly, this information must be supplied in a way making it tractable for computationally intensive satellite imagery processing systems operating on near real-time data streams. The approach taken here is based on a combination of theory and observations to produce a look-up table of lunar spectral flux at sufficiently high spectral resolution (1 nm) to make it applicable to a number of potential sensors. Auxiliary data pertaining to the sun/earth/moon geometry as a function of time provide the de-normalization information required to convert the data from mean-geometry values to ones applicable to a specific date and time.

4. THEORETICAL BASIS

Accurate representation of the TOA lunar spectral flux requires account for several factors: i) elliptical orbits of the earth and moon , ii) the lunar 'phase angle' (θ_p, related to what fraction of the moon appears illuminated when viewed from the earth), iii) intrinsic variations of the solar source, and iv) the heterogeneity of the lunar surface (both lunar surface properties and topography effects, e.g., crater shadows) which give rise to varying lunar reflectance with changing lunar phase angle and libration. Table 1 lists some geometric constants and other terms that are important to the calculation of lunar spectral flux.

Pertaining to elliptic orbits, the minimum and maximum S/E distances (perihelion and aphelion, respectively) lead to varying amounts of sunlight incident on the lunar surface, and the minimum and maximum moon/earth (M/E) distances (perigee and apogee, respectively) result in changes to the solid angle subtended by the moon. Since the moon is not a self-luminous object, the lunar radiance changes primarily according to the sun/moon distance, and the lunar flux upon the earth changes primarily according to earth-moon (E/M) distance.

An illustration of the lunar cycle in terms of phase angle, phase function, M/E geometry, and appearance of the moon as seen from Earth are shown in Fig. 1. These phase-angle-dependent variations in lunar brightness are taken into account with the 'phase function' [$f(\theta_p)$], which varies between 0 and 1 and describes the nonlinear behavior of lunar brightness with phase angle. For this work, curve-fits to the empirical data of Rougier (1933) for waxing and waning modes were used, shown in Figure 2.

The lunar spectral albedo (α_λ; integrated over the entire surface) shown together with the solar spectral flux (at 1AU) is shown in Figure 3. As the phase angle approaches 0° a reduction in crater shadows results in a non-linear increase in the apparent lunar brightness (~40% increase between 4° and 0°)—a phenomena known as the opposition surge (e.g., Buratti et al, 1996). The total solar irradiance as measured at one astronomical unit (AU; see Table 1) is roughly 1366 W/m^2, but varies in fact between 1360 and 1369 W/m^2 owing to fluctuations within the photosphere of the sun (e.g., the 11-year sunspot cycle). The primary variation in TOA down-welling solar irradiance is due to Earth's elliptical orbit, which results in an approximately +/- 3.4% spread about the solar constant (ranging between 1320 and 1412 W/m^2) over the course of the year.

Of note is the low value of mean lunar albedo (0.116; integrated between 0.4 and 0.7 μm and weighted/normalized by solar spectral flux)—surprisingly less than that of Earth (0.30). The moon being perceived as a very bright object in the nighttime sky is in fact the result of its strong contrast against the dark (space) background.

To derive the TOA lunar spectral flux, we begin with the solar source, whose irradiance (E;

defined as power P per unit area) at any point on the sphere defined by radius R is specified by:

$$E = \frac{P}{4\pi R^2}.$$ (1)

The solar irradiance at the mean S/E radius (i.e., when $R = \overline{R}_{se}$) follows as:

$$E_o = \frac{P}{4\pi \overline{R}_{se}^2}.$$ (2)

Combining Eqs. 1 and 2 to eliminate P, the solar irradiance at arbitrary S/E distance is expressed in terms of the solar constant, E_o:

$$E = E_o \left(\frac{\overline{R}_{se}}{R_{se}} \right)^2.$$ (3)

Analogous to Eq. 3, the solar irradiance incident upon the moon at arbitrary sun-moon distance is given by:

$$E_m = E_o \left(\frac{\overline{R}_{se}}{R_{sm}} \right)^2,$$ (4)

where R_{sm} is the sun-moon distance (varying over lunar cycle and season). This incident irradiance is reflected by the moon according to the geometric lunar albedo (α), producing an equivalent isotropic radiance, I_m:

$$I_m = \frac{\alpha E_m}{\pi}$$ (5)

which is then integrated over solid angle of the illuminated portion (phase dependent; as viewed from the earth) of the lunar disk to compute the final down-welling lunar flux.

Assuming for the moment the special case of a full moon with $\theta_m = 0°$ (and neglecting lunar eclipse effects), the down-welling TOA lunar spectral flux follows as the product between the lunar radiance and the solid angle subtended by the full lunar disc:

$$E_{TOA} = I_m \Omega_m = \left(\frac{\alpha E_m}{\pi} \right) \left(\frac{\pi r_m^2}{(R_{me} - r_e)^2} \right) = \alpha E_o \left(\frac{\overline{R}_{se}}{R_{sm}} \right)^2 \left(\frac{r_m}{R_{me} - r_e} \right)^2$$ (6)

Here, we consider the distance between the moon and the surface of the earth (= $R_{me} - r_e$) and R_{sm} is the center-of-mass sun-moon distance. For a full moon, R_{sm} is just the sum of the S/E and M/E distances, such that Eq. 6 becomes:

$$E_{TOA} = \alpha E_o \left(\frac{\overline{R}_{se}}{R_{se} + R_{me}} \right)^2 \left(\frac{r_m}{R_{me} - r_e} \right)^2.$$ (7)

In a more general sense, we can consider the varying lunar phase as a scaling of the maximum possible lunar spectral flux (for a given S/E/M geometry) by introducing to Eq. 7 the phase function, f:

$$E_{TOA} = \alpha E_o \left(\frac{\overline{R}_{se}}{R_{sm}} \right)^2 \left(\frac{r_m}{R_{me} - r_e} \right)^2 f(\theta_p) \quad ; \quad f \in [0,1]$$ (8)

where R_{sm} is the sun-moon distance, varying as a function of the lunar phase angle. Eq. 8 can be expressed in units of per-wavelength by using the spectrally-resolved values for albedo, solar flux, and the phase function.

5. COMPARISON TO LUNAR OBSERVATIONS

Calculations of lunar spectral flux by the model described above were compared against a collection of low-earth-orbiting satellite imaging radiometer moon-views. Given the very high photometric stability of the lunar surface (~10^6 yr; Kieffer, 1997), the moon represents an excellent target for vicarious calibration. Lunar views are collected monthly for on-orbit calibration purposes by instruments such as the Sea-viewing Wide Field-of-view Sensor (SeaWiFS; e.g., Barnes et al., 1999 and Eplee et al., 2004) and MODIS (e.g., Sun et al., 2003). Similar plans to use lunar reflectance as a calibration reference for the future NPOESS/VIIRS sensor visible and near-infrared bands are already in the works (Patt et al., 2005). Figure 4 shows percent-difference comparisons between observed and predicted (via the current work) lunar spectral radiances for an assortment of MODIS and SeaWiFS lunar calibration measurements. The various symbols denote different lunar phase angles regimes, partitioned into 15° increments, and are positioned on central wavelength of the satellite instrument bands. For the model calculations, the lunar solid angle was adjusted to match satellite altitude (i.e., substitution of moon-spacecraft distance for M/E distance). Typical agreement is within 5%, with slightly better performance observed for the low lunar phase angle cases, and are considered reasonable in light of there being no corrections/adjustments made to the observations to account for libration and sensor over-sampling effects (e.g., Eplee et al., 2004). There do not appear to be any significant wavelength or lunar phase angle biases, although MODIS comparisons do indicate a systematic positive bias (satellite radiances brighter than predicted). Comparisons against calculations of the RObotic Lunar Observatory (ROLO; Keiffer and Stone, 2005) are also underway.

5. STANDARD TABLE

Since the intent of the lunar spectral flux model is for near real-time processing, we require a practical and computationally efficient means to specifying the down-welling TOA lunar irradiance. For this purpose we are preparing a set of look-up tables referenced to a standard S/E/M geometry and appealing to an auxiliary dataset of time-dependent parameters for scaling the results to the current S/E/M geometries.

The standard tables were defined for mean S/E distance (1 AU) and mean M/E distance (see Table 1). The only degree of freedom is the varying position of moon (i.e., the varying lunar phase angle). Libration effects are neglected. If the standard look-up table (using geometry) can be represented following the same construct as Eq. 8:

$$\overline{E}_{TOA} = \alpha E_o \left(\frac{\overline{R}_{se}}{\overline{R}_{sm}} \right)^2 \left(\frac{r_m}{\overline{R}_{me} - r_e} \right)^2 f(\theta_m) \quad , \quad (9)$$

then the adjustment factor used to convert from standard distances to a current S/E/M geometry is the ratio between Eq. 8 and Eq. (9):

$$F = \left(\frac{\overline{R}_{sm}}{R_{sm}} \right)^2 \left(\frac{\overline{R}_{me} - r_e}{R_{me} - r_e} \right)^2 \quad . \quad (10)$$

Provided tables of lunar phase angle, S/E distance, and M/E distance as a function of time, the current sun-moon distance may be calculated via Pythagorean's theorem as follows:

$$R_{sm} = \sqrt{(R_{se} + R_{me}\cos(\theta_p))^2 + (R_{me}\sin(\theta_p))^2} \quad , \quad (11)$$

and the corresponding mean value (for a given phase angle) follows as:

$$\overline{R}_{sm} = \sqrt{(\overline{R}_{se} + \overline{R}_{me}\cos(\theta_p))^2 + (\overline{R}_{me}\sin(\theta_p))^2} \quad . \quad (12)$$

Since the distance between the moon and earth is very small compared to the distance between either and the sun, Eq. 10 can be rewritten to good approximation in a form that is independent of the lunar phase angle:

$$F = \left(\frac{\overline{R}_{se}}{R_{se}} \right)^2 \left(\frac{\overline{R}_{me} - r_e}{R_{me} - r_e} \right)^2 \quad . \quad (13)$$

The standard tables were calculated at 1° resolution in lunar phase angle. Results for selected lunar phase angles are shown in Fig. 5, along with the VIIRS DNB spectral response function (SRF). Correction terms (Eq. 10) corresponding to the extreme conditions of apogee/aphelion and perigee/perihelion applied to the bold standard curves show the possible spread in the solution space arising from variable S/E/M geometry. A comparison of the exact and standard lunar flux at 600 nm for the waxing mode of the lunar cycle, shown in Fig. 6 (for a case near mean S/E/M geometry), confirms close agreement (within 0.05%) even after the approximation introduced in Eq. 13.

The standard table can be applied to any date/time provided knowledge of the current S/E distance, M/E distance, and lunar phase angle. An auxiliary dataset of hourly values for these quantities has been computed and will be supplied with the standard tables. The general procedure for applying these tables to a sensor with arbitrary SRF (confined to the valid spectral interval [0.2, 2.8 μm]) is as follows: (i) given the current date and time, interpolate the auxiliary dataset to obtain the corresponding S/E,M/E distances and lunar phase angle information, (ii) linearly interpolate the 1-degree standard lunar spectral flux tables according to the phase angle determined in step (i), (iii) scale the standard spectral flux according to the current S/E, M/E distances interpolated in step (i) using Eq. 13, and finally, (iv) convolve the interpolated/scaled lunar spectral flux data with a normalized SRF to yield a sensor-specific TOA lunar flux, e.g.,

$$E_{TOA,DNB} = \left. \int_\lambda E_{TOA}(\lambda)\phi(\lambda)d\lambda \middle/ \int_\lambda \phi(\lambda)d\lambda \right. \quad (23)$$

5. APPLICATIONS

A number of potentially valuable nighttime applications become possible with the availability of a lunar spectral flux dataset, including the following:

1) Cloud cover detection (example where night vis sees it and conventional IR does not) based on visible reflectance thresholds, including cloud overlap regimes following the daytime approach of Pavolonis and Heidinger (2004). Figure 7 illustrates this concept.
2) Surface characterization (e.g., including snow cover and sea ice detection and mapping) via lunar reflectance thresholds.
3) Aerosol (dust/smoke/volc ash) detection and properties (e,g, Zhang et al., 2008) .
4) Cloud/aerosol optical depth retrievals, e.g., conventional over water or in/out of cloud shadows over land.

In terms of existing NPOESS EDRs that would benefit from the addition of DNB information, compelling arguments can be made for several:

1) VIIRS-Only: imagery, surface albedo, cloud base height, cloud cover/layers, cloud effective particle size, cloud optical thickness, cloud top height, cloud top pressure, cloud top temperature, surface type, aerosol optical thickness (input of lunar reflectance to radiative transfer models)
2) VIIRS+Microwave Imager/Sounder (MIS): imagery, sea ice, snow cover (lunar reflectance thresholds)
3) Space Environmental Sensor Suite (SESS): auroral boundary and auroral energy deposition (filtering out cloud/surface contamination from auroral scenes)

Nighttime application development in these and other areas in conjunction with the current research are ongoing at the Naval Research Laboratory in Monterey, CA, and the Cooperative Institute for Research in the Atmosphere (CIRA) in Fort Collins, CO.

6. CONCLUSION

A model capable of producing lunar spectral irradiances at 1 nm spectral resolution between 0.2 and 2.8 μm has been developed to enable quantitative applications of the VIIRS Day/Night Band. To make its usage computationally tractable, we produced a standard look-up table based on mean S/E and M/E distances together with auxiliary data tables used to adjust the standard S/E/M geometry results to the specific-geometry of current observations. After convolving the spectra with the DNB SRF, a sensor-weighted TOA down-welling lunar spectral flux value can be used in a way that is analogous way to the down-welling TOA solar spectral flux (i.e., enabling the computation of scene reflectance, which is used for a variety of cloud/aerosol/surface quantitative applications).

The first VIIRS-DNB sensor will be included on the NPOESS Preparatory Project (NPP), slated for launch in late 2009. As implied by its name, the purpose of the NPP is to serve as risk reduction for the novel suite of NPOESS sensors, and affording the user community a first opportunity to explore the new capabilities and thereby prepare for the future operational data stream. Similar to previous satellite observing systems such as MODIS, SeaWiFS, and the Advanced Microwave Scanning Radiometer (AMSR-E), however, the NPP will in all likelihood be leveraged for operational support purposes. As such, a goal of this research was to supply a lunar dataset in advance of the NPP demonstration program. The lunar spectral flux database, auxiliary data, and a README instruction file will be made available shortly (in conjunction with Miller and Turner, 2008).

10. REFERENCES

Barnes, R. A., R. E. Eplee, Jr., F. S. Patt, and C. R. McClain, 1999: Changes in the radiometric sensitivity of SeaWiFS determined from lunar and solar-based measurements, Robert A. Barnes, Robert E. Eplee, Jr., Frederick S. Patt, and Charles R. McClain, Appl. Optics, 38, 4649-4664.

Buratti, B. J., J. K. Hillier, and M. Wang, 1996: The lunar opposition surge: observations by Clementine. *Icarus*, **124**, 490-499.

Croft, T. A., 1978: Nighttime images of the earth from space. Sci. Amer., **239**, 68-79.

Elvidge, C. D., K. E. Baugh, J. B. Dietz, T. Bland, P. C. Sutton, and H. W. Kroehl, 1999: Radiance calibration of DMSP-OLS low-light imaging data of human settlements. *Rem. Sens. Env.*, **68**, 77-88.

Eplee, R. E., Jr., R. A. Barnes, F. S. Patt, G. Meister, and C. R. McClain, 2004: SeaWiFS lunar calibration methodology after six years on orbit, *Proc. SPIE*, **5542-2**, 13 pp.

Kieffer, H. H., 1997: Photometric stability of the lunar surface. *Icarus*, **130**, 323-327.

Kieffer, H. H., and T. C. Stone, 2005: The spectral irradiance of the moon. *Astron. J.*, **129**, 2887-2901.

Lee, T. F., S. D. Miller, F. J. Turk, C. Schueler, R. Julian, S. Deyo, P. Dills, and S. Wang, 2006: The NPOESS/VIIRS day/night visible sensor, *Bull. Amer. Meteor. Soc.*, **87**(2), 191-199.

Lee, T. F., F. J. Turk, and K. Richardson, 1997: Stratus and fog products using GOES-8-9 3.9 µm data. Wea. Forecasting, 12, 664-677.

Miller, S. D., and R. E. Turner, 2008: A Dynamic Lunar Spectral Flux Dataset for NPOESS/VIIRS Day/Night Band Environmental Applications, Submitted to IEEE Trans. Geosci. Rem. Sens.

Pavolonis, M.J. and A.K. Heidinger, 2004: Daytime cloud overlap detection from AVHRR and VIIRS. *J. Appl. Meteor,* **43**, 762-778.

Patt, F. S., R. E. Eplee, R. A. Barnes, G. Meister, and J. J. Butler, 2005: Use of the moon as a calibration reference for NPP VIIRS. *Proc. SPIE*, **5882-43**, 12pp.

Rougier, A., 1933: Total photoelectric photometry of the Moon. *Ann. Obs. Starsbourg*, **2**, 205-339.

Sun, J., X. Xiong, B. Guenther, and W. Barnes, 2003: Radiometric stability monitoring of the MODIS solar reflective bands using the Moon. *Metrologia*, **40**, S85-S88, 2003.

Zhang, J., J. S. Reid, S. D. Miller, and F. J. Turk, 2008: Strategy for studying nocturnal aerosol optical depth using artificial lights. *Int. J. Rem. Sens.*, In press.

Parameter	Symbol	Value and Units
Sun Radius	r_s	695,508 km
Moon Radius	r_m	1737.4 km
Earth Radius (Equatorial)	r_e	6378.14 km
Moon/Earth Perigee Distance	$R_{me,p}$	356,371 km
Moon/Earth Apogee Distance	$R_{me,a}$	406,720 km
Sun/Earth Perihelion Distance	$R_{se,p}$	147,088,067.2 km
Sun/Earth Aphelion Distance	$R_{se,a}$	152,104,233.4 km
Astronomical Unit	AU	149,597,870.7 km
Mean Sun/Earth Radius	$\overline{R}_{se}$	149,598,022.6 km
Mean Moon/Earth Radius	$\overline{R}_{me}$	384,401 km
Lunar Visual Albedo	ρ	0.116; $0.105 < \rho < 0.125$
Total Solar Irradiance	E_o	1366.1 W/m^2 (at 1AU); $1360 < E_o < 1369$ W/m^2

Table 1: Constants used in calculation of lunar spectral flux. All distances between bodies are from center-of-mass to center-of-mass. (From Miller and Turner [2008])
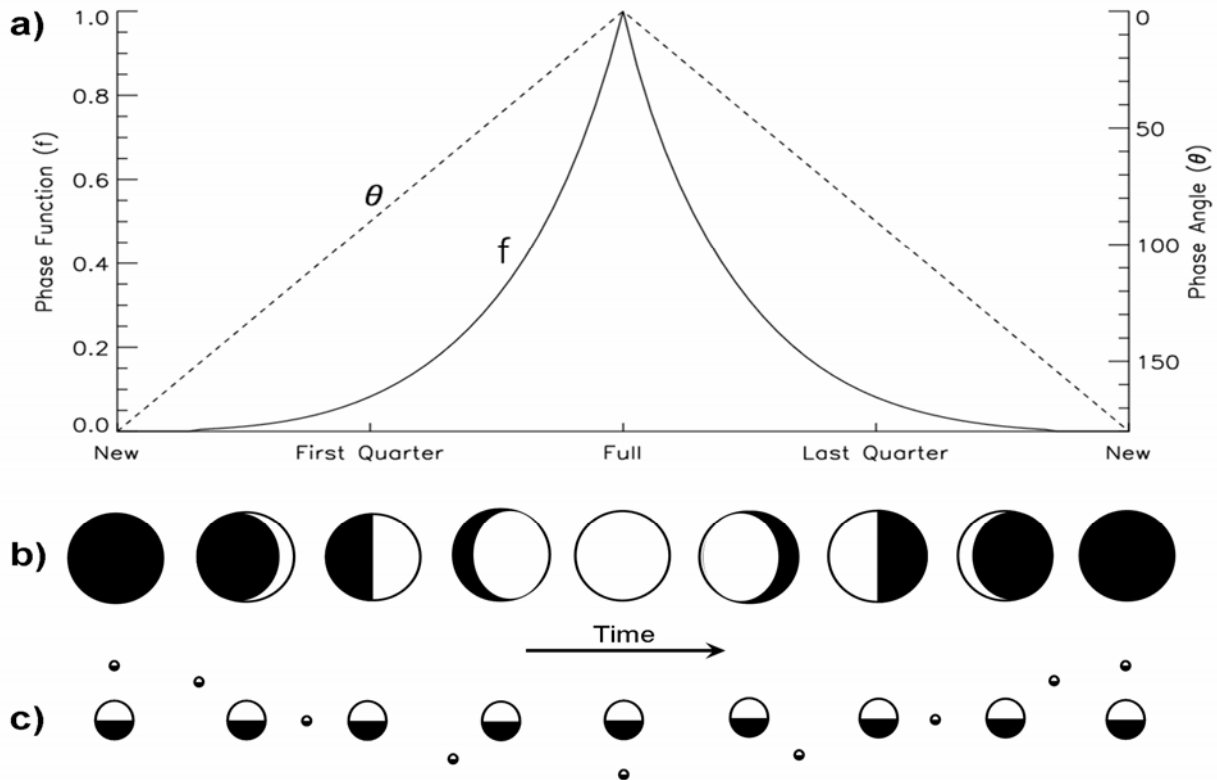
Figure 1: (a) Evolution of the lunar phase angle (θ) and phase function (*f*) over the course of the lunar cycle, (b) changing appearance of the lunar disk as seen from Earth, (c) Earth/Moon geometry (not drawn to scale) as viewed from a position above the north pole of Earth (with sunlight originating from top of page). In b-c, illuminated sides of bodies are shown in white and shaded sides in black. (From Miller and Turner [2008])
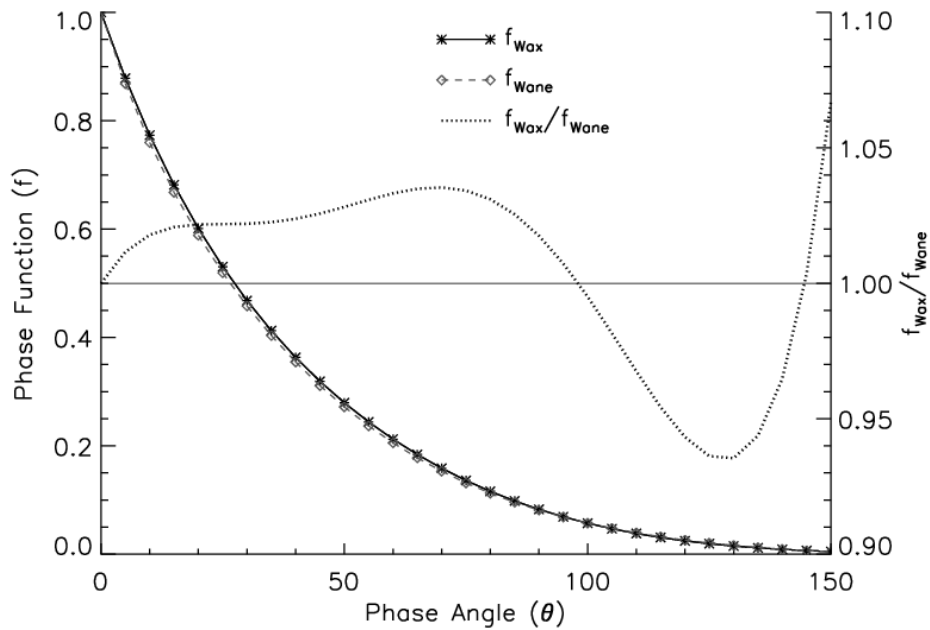
Figure 2: The waxing and waning lunar phase functions, fitted to observational data from Rougier (1933), with differences between the two plotted as a function of phase angle. (From Miller and Turner [2008])
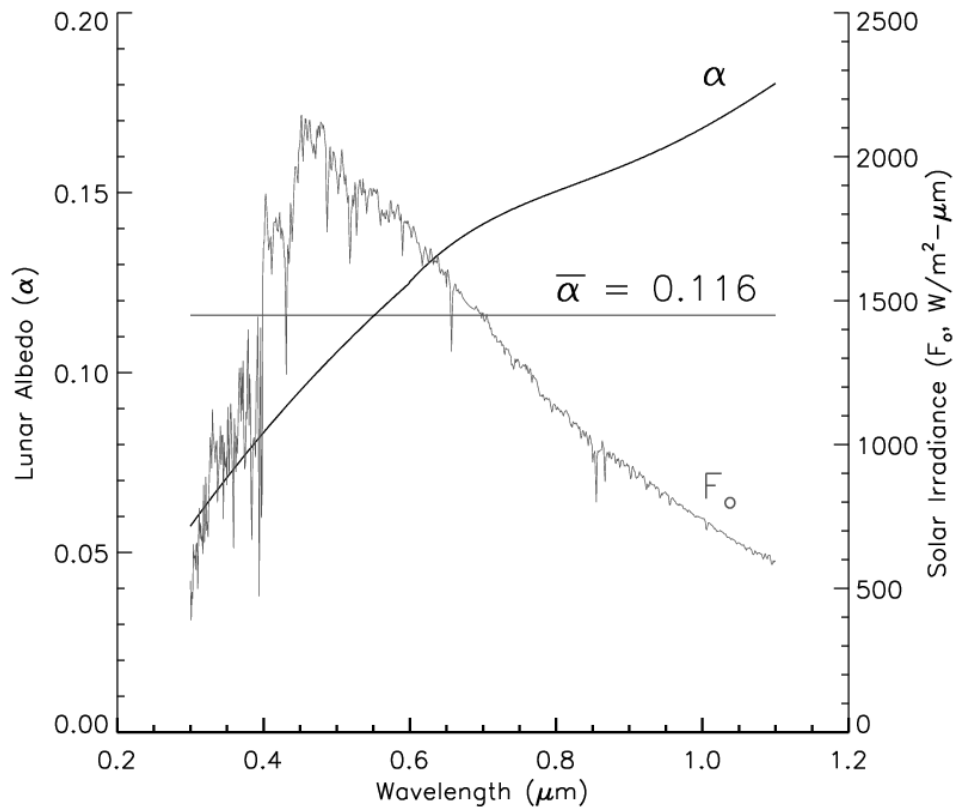

Figure 3: Solar spectral flux (F_o) and spatially averaged lunar spectral albedo (α) across the visible and shortwave infrared. The spectral mean value of α (shown as horizontal line) is weighted by F_o. (From Miller and Turner [2008])
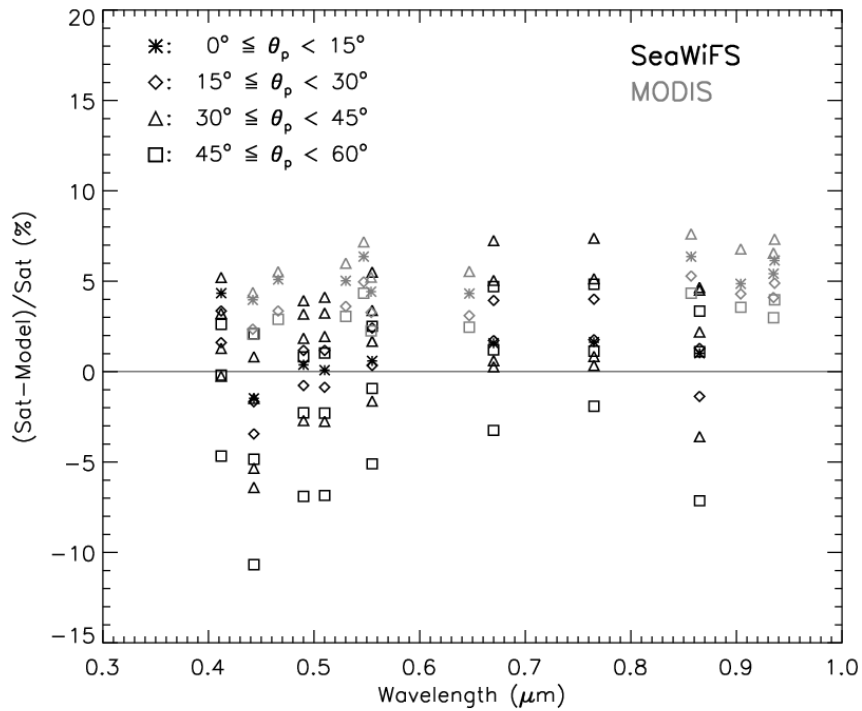
Figure 4: Comparisons between the current model and lunar-views by SeaWiFS (black symbols) and Aqua MODIS (gray symbols) for selected sensor bands across the visible and shortwave infrared. Symbols correspond to different lunar phase angle regimes ranging roughly from gibbous to nearly-full. (From Miller and Turner [2008])
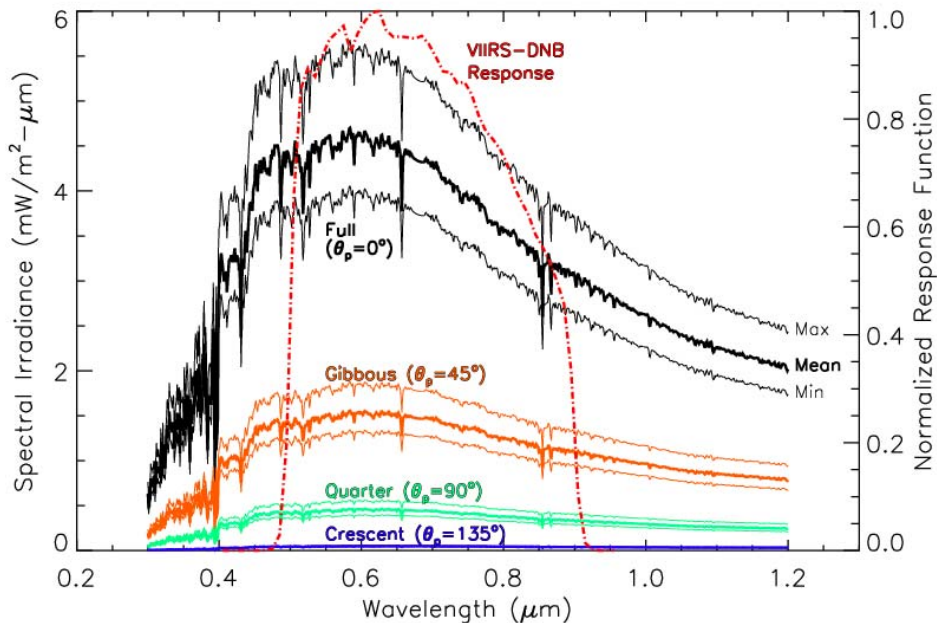

Figure 5: Results from the standard lunar spectral flux tables for selected lunar phase angles ranging from crescent to full-moon. Heavy curves ("Mean") correspond to the standard geometry (1 AU, mean moon-earth distance). Light curves ("Max" and "Min") correspond to perigee/perihelion and apogee/aphelion geometries, respectively. The VIIRS DNB spectral response function (courtesy Raytheon Santa Barbara Remote Sensing) is shown as a red dashed-dot curve. (From Miller and Turner [2008])
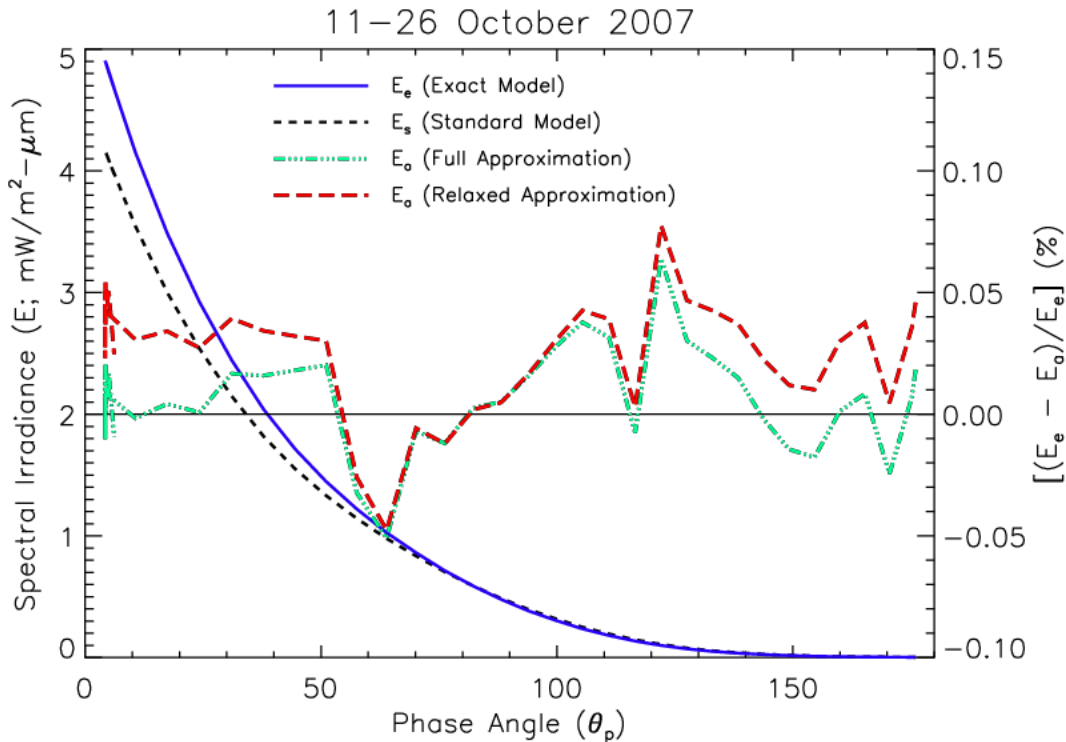
Figure 6 Left ordinate: comparison between the standard (using mean sun-earth and earth-moon distances) lunar flux model and exact calculations at λ=600 nm for the waxing moon over 11-26 October 2007. Right ordinate: percent-differences between exact and adjusted-standard models using the conversion factors described in the text. (From Miller and Turner [2008])
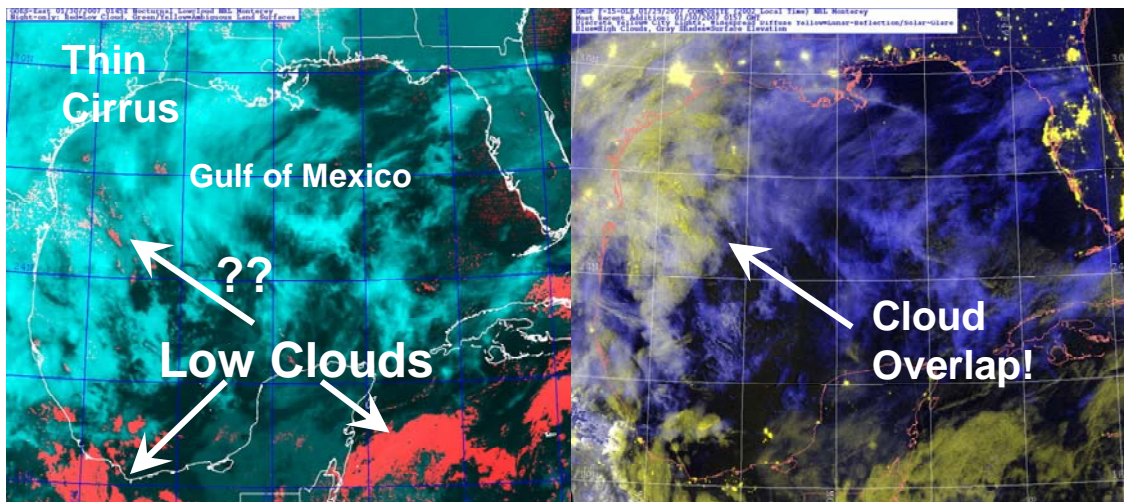

Figure 7 A qualitative example of how a high-over-low cloud overlap region is detected via moonlight reflectance when combined with other near-infrared and thermal-infrared information. In the left panel, a low cloud detection product (e.g., Lee et al. [1997]) based on the 3.7 – 11.0 μm brightness temperature difference enhances un-obscured low clouds in red tonality, while overriding cirrus is shown in cyan. In the right panel, moonlight reflectance from the OLS, combined with the infrared channel on OLS, reveals an 'anomalous bright region' beneath the cirrus shield corresponding to an infrared-obscured low cloud deck. Appropriate visible reflectance (lunar) thresholding would allow for an improved nighttime cloud mask based on moonlight data. (Adapted from Miller and Turner [2008])